Journal of Petroleum Geology

WILEY

ORIGINAL ARTICLE

Laminated Shale nm–μm-Scale Pore System Structure, Fractal Dimensions and Its Controlling Factors of the Paleocene Shahejie Formation: Evidences From CO_2 Adsorption and N_2 Adsorption Experiments

Biao Sun[1,2,3] | Xiaoping Liu[1,2] | Xiaoguang Li[4] | Yongcheng Chen[4] | Chang Chen[4] | Tian Liu[1,2] | Zilong Zhang[1,2] | Wenhui Xie[1,2] | Murray Gingras[3]

[1]State Key Laboratory of Petroleum Resources and Engineering, China University of Petroleum (Beijing), Beijing, China | [2]College of Geosciences, China University of Petroleum (Beijing), Beijing, China | [3]Department of Earth and Atmospheric Sciences, University of Alberta, Edmonton, Canada | [4]Research Institute of Petroleum Exploration and Development, Liaohe Oil Field Company, PetroChina, Panjin, Liaoning, China

Correspondence: Xiaoping Liu (liuxiaoping@cup.edu.cn)

Revised: 10 January 2026 | **Accepted:** 19 January 2026

Keywords: CO_2 adsorption | controlling factors | laminated shale | N_2 adsorption | pore system structure

ABSTRACT

Characterizing the pore system of shale oil reservoirs is critical to elucidating petroleum accumulation mechanisms, enhancing oil recovery efficiency, and evaluating unconventional petroleum resources. However, research on lacustrine laminated shale pore systems remains limited and poorly understood, primarily constrained by the strong heterogeneity induced by differential lamina development. To address this gap, we collected 20 lacustrine shale samples from the fourth member of the Shahejie Formation in the Bohai Bay Basin and systematically investigated their nm–μm scale pore structure using CO_2 and N_2 adsorption experiments. The results show that the laminated shales are composed of light-colored mineral-rich layers (quartz, feldspar, calcite, and dolomite) alternating with dark clay–organic matter layers. Their pore system is dominated by matrix intercrystalline, intergranular, dissolution pores, and microfractures, rather than organic-matter-associated pores, with pore diameters primarily ranging from 2 to 40 nm. Notably, mesopores account for over half of the total specific surface area and pore volume in all tested samples, and the abundance of clay and quartz minerals is identified as the key factor controlling micro–mesopore composition and complexity. These findings provide critical insights for understanding shale oil resource potential and delineating optimal exploitation targets in lacustrine basins.

1 | Introduction

As traditional resource consumption and reserves diminish while energy demand continues to increase, unconventional resources, such as shale oil, have become the primary focus of exploration. Globally, the projected recoverable reserves of shale oil resources are around 1.4×10^{12} tons, which is almost triple the entire amount of conventional oil reserves [1–6]. Despite this vast potential, successful oil extraction from oil-bearing shale reservoirs is currently estimated to be under 10% [7–10]. The lack of geological data and a number of engineering aspects make it difficult to understand important characteristics that are necessary for assessing oil recovery.

It is well known that determining the resource potential of oil deposits requires an understanding of the structure of the shale

pore system. The pore system also significantly influences the identification and evaluation of favorable locations, known as sweet spots, as oil flows more easily through laminated pore systems [11–14]. Therefore, comprehending the pore system in laminated shale and the influencing factors is vital for gaining deeper insights into the complexities of shale oil exploitation. There are various evaluation methods available for assessing the characteristics of the pore structure in lacustrine shale reservoirs. The commonly used methods include image analysis, experimental testing methods, and geometric fractal methods [15–19]. Each method comes with its unique strengths and drawbacks. Core scanning electron microscopy allows for the immediate observation of pore-throat characteristics at various scales, but it falls short in quantitatively characterizing pore-throat size and distribution characteristics. The N_2 adsorption method provides accurate characterization of the meso–macropore structure, with a maximum pore diameter (PD) of 300 nm [20–22]. Low-temperature CO_2 adsorption precisely determining and defining the micropore (<2 nm) structure. The mercury injection method has demonstrated greater effectiveness in assessing macropore (>120 μm) structure, but high pressure may change the sample's pore structure [23–25]. Nuclear magnetic resonance experiments are effective in determining the lower limit of movable oil. However, the test signal strength is easily influenced by mineral components, organic matter, and so forth, and the resulting pore size distribution values need to be converted to obtain accurate measurements [26–28]. The full pore size properties of shale are frequently characterized using multi-method integrated analysis [29, 30]. The most popular technique for evaluating the irregularity of pore structures and surfaces in coal, marine shale, and lacustrine shale is the use of fractal dimension obtained from N_2 adsorption data [31, 32]. However, there has been limited research on analyzing the fractal pore characteristics within the laminated shale pore system.

In previous studies, numerous researchers focused on elements such as fluid level, temperature, pressure, microbial activity, mineral types, hydrocarbon production qualities, and a variety of other factors that have been shown to influence pore system structure and fractal dimensions [33–37]. Generally speaking, organic pores are more likely to develop in the reheating evolution of organic matter microscopic components with high hydrogen-rich components. In addition, with the increase of organic matter abundance, organic pores are increasingly developed, but the high-maturity kerogen causes some organic pores to close and disappear due to shrinkage metamorphism, and the organic pores are mainly irregular and rough surfaces, which have a destructive effect on the pore structure [38–43]. The study also found that as clay minerals have a constructive effect on PD and fractal, it is mainly because clay minerals have better ductility, which makes it difficult to form larger pores during diagenesis, or the original large pores are squeezed and disappear by compaction, resulting in an increase in interlayer pores [44–47]. In addition, the water film formed on the clay minerals' surface causes the fractal dimension to decrease [48]. Previous studies further believed that with the increase of the quantity of brittle minerals, like siliceous minerals and carbonates, the total pore volume (TPV) gradually increases, mainly because brittle minerals have high compressive strength and are also dissolved by acid to produce a large amount of storage space, but it is worth noting that the pores between brittle mineral particles are often filled with clay minerals and organic matter, causing deformation of the macropore structure, resulting in enhanced macropore heterogeneity [49–52].

The lamina structure is a unique structural feature of laminated shale, and its double-layer structure of hydrocarbon generation layer and reservoir layer significantly affects the allocation of the pore structure system. There haven't been research studies done on the laminated shale pore system structure, fractal dimensions, and its controlling factors. This study attempts to perform a quantitative examination of shale oil, with a particular focus on the pore system structure at the nm–μm scale in laminated shale, its fractal dimensions, and the factors that control these characteristics within laminated shale reservoirs. The investigation employs various methods and tools, including x-ray diffraction, total organic carbon (TOC), vitrinite reflectance (Ro), scanning electron microscopy, low-temperature nitrogen adsorption, and CO_2 adsorption. The research is based primarily on laminated shale samples from the Paleogene Shahejie Formation in the Bohai Bay Basin, East China, to analyze the pore system structure, fractal dimensions, and relevant controlling factors. The results advance our knowledge of the pore system structure in organic-rich layered shale. It is essential for future shale oil exploration and the expansion of the industry as a whole.

2 | Geological Setting

The northernmost part of the Bohai Bay Basin is home to the Damintun Sag (Figure 1A), encompasses a substantial region of approximately 800 km^2 and is a significant component of the greater Liaohe Sag [53, 54]. This Cenozoic continental rift basin, formed on ancient basement rock formations, exhibits distinctive structural features characterized by a "three concave and seven convex" pattern (Figure 1B). The structural depressions across this basin include the Santaizi, Anfutun, and Rongshengbao depressions (Figure 1C). During the Paleogene period, the basin was primarily composed of the Dongying and Shahejie Formation, with the latter formation is further divided into four distinct sections (Figure 1D). Notably, sequence characteristics enabled the Shahejie Formation to be divided into three submembers. The Es_4 that is situated at the base of the formation indicates the deposition of the lake environment during the maximum lake transgression; lake depositional systems were the main depositional systems, with some areas experiencing deltaic depositional systems. It was evident that within the basin, there was extensive development of sediments ranging from deep lake to semi-deep lake subfacies, which collectively formed a mixture of shale, carbonate, and siltstone [55]. Sedimentary thickness varies from 30 to 200 m, with organic-rich shale predominantly found in Anfutun and the central uplift zone. Given these observations, the study area represents not only a vital source of conventional resources but also a vital resource for substantial shale oil and gas.

3 | Materials and Methods

3.1 | Sample Collection

Twenty shale core samples in all were extracted from the Es_4 interval of newly drilled Well S, as depicted in Figure 1C. These samples were taken from depths ranging between 3530.75 and

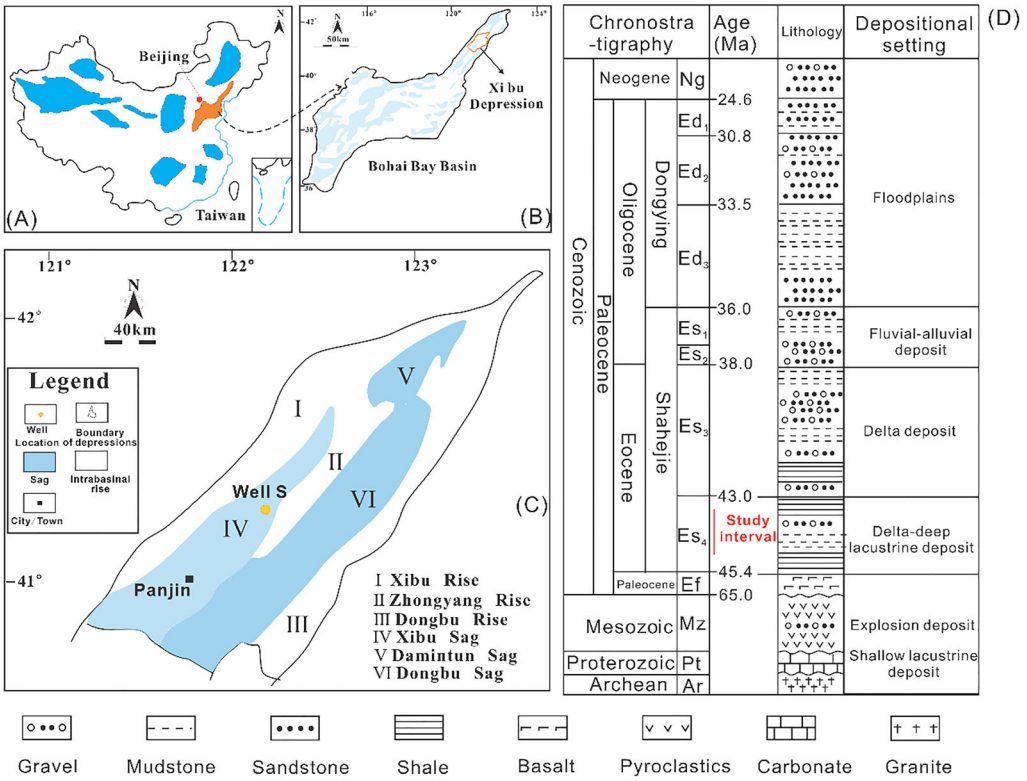

FIGURE 1 | The maps showing (A) the locations of the Bohai Bay Basin; (B) the secondary tectonic units and location of the Liaohe Depression; (C) the location of well S for core samples; and (D) the diagram showing the stratigraphic compositions, main lithology, and depositional setting.

3708.42 m. The Es_4 was formed in a lacustrine environment. Each of the 20 shale samples has laminas and is either dark gray or black in appearance. Various analyses were performed on the samples, including x-ray diffraction, thin section analysis, TOC, Ro, scanning electron microscopy, and low-temperature N_2 and CO_2 adsorption. The experimental diagram can be found in Figure 2.

3.2 | Experimental Methods

3.2.1 | X-Ray Diffraction, Thin Section Analysis, and Scanning Electron Microscopy

The collected samples were grinded into a fine powder to ensure a homogeneous and random orientation of crystallites. The prepared samples were put onto the sample holder of the Bruker D2 PHASER instrument to ensure the sample is properly aligned and centered in the x-ray beam path. Set the x-ray source parameters (30 kV, 10 mA) according to the instrument specifications and sample requirements. After the scan is complete, analyze the diffraction pattern using the Rietveld refinement procedure to precisely ascertain the samples' mineral compositions.

Cut a small, representative piece of the sample using a rock saw. Glue the cut sample onto a glass slide using epoxy resin and allow it to cure. Grind the mounted sample to a thickness of about 30 μm using a series of abrasive papers, then polish it to a smooth finish. Place the prepared slide on the microscope stage, and then analyze it at magnification settings ranging from 20× to 400× under both single and orthogonal polarizations. Take notes on the observed structures, textures, and any other relevant characteristics.

Place the mounted sample into the argon ion polishing chamber. Ensure that the sample is positioned correctly for uniform polishing. Start the ion polishing process with the Ilion 697 machine. The ion beam will gradually remove surface layers, creating an ultrasmooth and damage-free surface. Clean the sample surface gently using compressed air to remove any residual particles or contaminants. Use low magnification to locate the area of interest on the polished surface. Switch to higher magnifications for detailed imaging of the ultrasmooth surface with the field emission scanning electron microscope FEI Quanta FEG450.

3.2.2 | TOC and Ro

Use a jaw crusher to break up the shale samples into small pieces, then grind them into a fine powder using a ball mill or mortar and pestle. The particle size should be less than 200 mesh (75 μm) to ensure homogeneity. To avoid any moisture interfering with the analysis, dry the powdered sample for 24 h at 60°C. Weigh approximately 100–200 mg of the dried shale powder and place it in a beaker or reaction vessel. Add 10% hydrochloric acid (HCl) to the sample to dissolve carbonate minerals (e.g., calcite and dolomite) and remove inorganic carbon. Allow the reaction to proceed at room temperature for a full day. An oven with a temperature range of 60–80°C was used to dry the samples. Calculate the TOC content of shale, typically reported as a weight percentage (wt%).

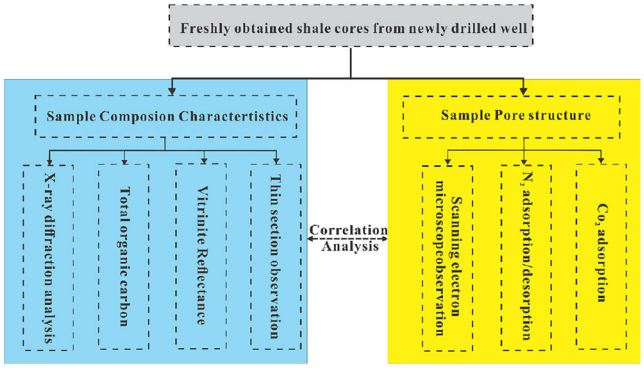

FIGURE 2 | Experimental block diagram of the study.

Crush the shale samples into small pieces using a jaw crusher, then grind them into a fine powder using a ball mill or mortar and pestle. Mix the powdered sample with epoxy resin and allow it to cure. Use the microscope to locate vitrinite particles within the shale sample. Measure the reflectance of the vitrinite particle using the MSP 400 instrument. Measure the reflectance of at least 50 vitrinite particles to ensure statistical reliability.

3.2.3 | N_2 Adsorption

Degas the sample to remove any adsorbed contaminants or moisture. Calibrate the Micromeritics ASAP 2460 instrument. Ensure the system is leak-free and properly evacuated. Fill the sample chamber with regulated quantities of nitrogen gas in incremental steps. At each equilibrium point, measure the volume and pressure of nitrogen gas that the sample has adsorbed. Gradually reduce the pressure in the system to allow the adsorbed nitrogen to desorb from the sample. Record the pressure and volume of nitrogen desorbed at each step. Collect adsorption and desorption isotherms, which plot the amount of nitrogen adsorbed/desorbed versus the relative pressure (P/P_0). Utilizing models and the Barrett–Joyner–Halenda (BJH) technique for pore size analysis, compute surface area, pore size distribution, and pore volume based on the data gathered.

Prior to the experiment, the sample was degassed to remove adsorbed contaminants and moisture, which is a prerequisite for ensuring the accuracy of adsorption data. The Micromeritics ASAP 2460 instrument was calibrated first, followed by leak testing and thorough evacuation of the system to eliminate interference from residual gas. Subsequently, regulated quantities of nitrogen gas were introduced into the sample chamber in incremental steps; at each equilibrium point, the volume and pressure of nitrogen adsorbed by the sample were recorded. The system pressure was then gradually reduced to facilitate desorption of adsorbed nitrogen, with the pressure and volume of desorbed nitrogen documented at each step. Adsorption and desorption isotherms were generated by plotting the amount of nitrogen adsorbed/desorbed against relative pressure (P/P_0). For pore size analysis, the BJH technique was employed to calculate specific surface area (SSA), pore size distribution, and TPV, which is a widely accepted method for mesopore characterization in shale studies. In addition, the fractal dimension was calculated to quantify pore complexity, with the methodological details referring to the approach [56], ensuring the reliability and comparability of the fractal analysis results.

3.2.4 | CO_2 Adsorption

The carbon dioxide adsorption method was used to characterize the micropore structure (<2 nm). The carbon dioxide adsorption test used the Micromeritics ASAP 2460, a high-performance fully automatic gas adsorption instrument from Micromeritics, with a test temperature of 0°C and a test accuracy of ±0.1%. The micropore size distribution calculation model used was the improved nonlocal density function theory (NLDFT) model.

3.3 | Fractal Methods

The Frenkel–Halsey–Hill (FHH) fractal theory was used to provide the following assessment approach on the basis of the data from the N_2 adsorption experiment [57–62]:

$$\ln\left(\frac{V}{V_0}\right) = C + K \times \ln\left[\ln\left(\frac{P_0}{P}\right)\right] \quad (1)$$

where V is the gas adsorption volume (cm^3) at the equilibrium pressure P; K is the correlation coefficient of the fractal dimension D; and C is a constant; and V_0 is the saturation adsorption volume (cm^3) of the monolayer gas.

$$D = K + 3 \quad (2)$$

The primary method for calculating the fractal dimension (D) is to examine the slope K of the line connecting $\ln V$ and $\ln(P_0/P)$, where K is the slope of the fitted straight line, and D is the fractal dimension.

The D value for pore structure typically ranges from 2 to 3. A D value of 2 indicates an exceedingly smooth surface, whereas a D value of 3 indicates a rough surface with irregular topography and a space-filling structure. The plots were segmented into two parts on the basis of relative pressure ranges: 0–0.45 and 0.45–1.0, each representing distinct gas adsorption characteristics. The fractal dimensions were determined separately for each segment, denoted as $D1$ and $D2$.

4 | Results

4.1 | Mineral Compositions, TOC Content, and Thermal Maturity

Thin section observations suggest that the laminae are well developed (Figure 3). At sedimentary horizontal planes, the laminated structure exhibits abrupt variations in grain size, color, and mineral content. The laminae, found in the shales, are predominantly rich in clay, organic matter, carbonate, and sand. There are three types of laminae combinations: organic-rich laminae + carbonates laminae, clay-rich laminae + sandy laminae, and sandy laminae + organic-rich laminae + carbonates laminae. The single carbonate lamination's thickness varies between 40 and 450 μm, according to an integrated analysis of

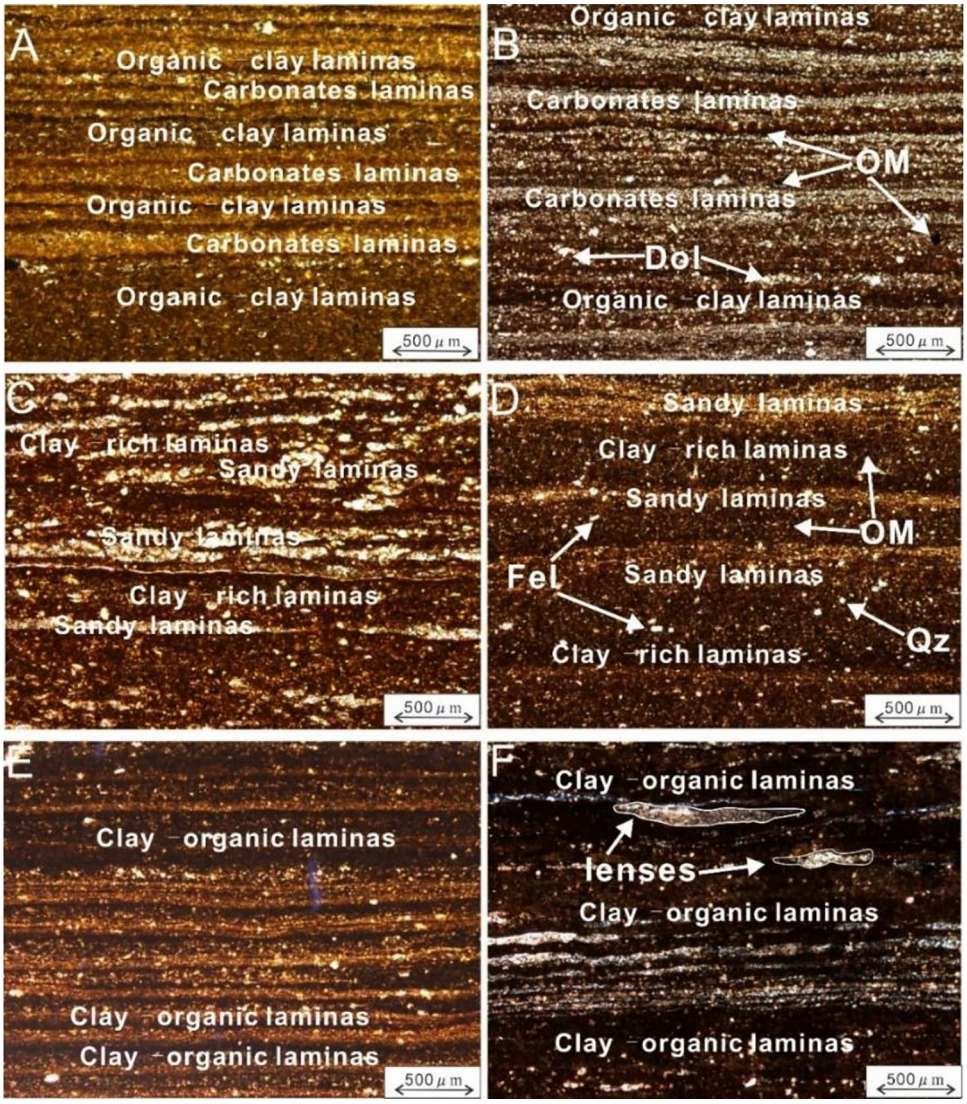

FIGURE 3 | Petrographic characteristics of the laminated shale in the fourth member Shahejie Formation from the Well S in the study area: (A) Thin sections showing the characteristics of clay–organic-rich laminas and carbonate laminas, Well S, 3615.30 m; (B) thin sections showing the dolomite separated with organic matter, Well S, 3654.33 m; (C) thin sections showing the characteristics of clay–organic-rich laminas and sandy laminas, Well S, 3660.53 m; (D) thin sections showing the distribution characteristics of feldspar, quartz, and organic matter in the laminas, Well S, 3670.2 m; (E) thin sections showing the characteristics of clay–organic-rich laminas, Well S, 3680.11 m; and (F) thin sections showing the characteristics of lenses filled with in clay–organic laminas, Well S, 3686.31 m.

polarizing microscope images (Figure 3A). The dark laminae primarily consist of organic matter and clay, whereas the light laminae are mainly dolomite (Figure 3B). In comparison to the organic–clay laminae, which range in thickness from 20 to 540 μm, the siliceous laminae typically have a thickness of 10–300 μm (Figure 3C). In addition, a few quartzes and feldspars are surrounded by organic matter and clay in the laminas (Figure 3D). Clay and organic materials make up the majority of the dark laminae (Figure 3E). There also develops a range of lenses in size from 500 to 950 μm (Figure 3F).

Table 1 displays the findings of the mineralogical study as determined by XRD. The mineral composition of the shale includes quartz, feldspar, clay, calcite, and dolomite. The shale samples have a greater clay concentration and are made up of carbonates and detrital minerals. The mineral composition exhibits substantial vertical heterogeneity. Specifically, carbonates are predominantly composed of calcite and dolomite, with average values of 21.18% and 9.52%, respectively. The carbonate content fluctuates widely, ranging from 5.5% to 54.3%, with an average of 30.70%. The shale samples had an average of 23.2% detrital mineral content (quartz and feldspar), and the clay content averages 37.6%.

TOC is necessary for hydrocarbon generation, with quantity levels being one of the most important predictors of the hydrocarbon-generation potential in rocks. The TOC of the Shahejie Formation collected from Well S is 2.51% on average, ranging from 1.05% to 5.83% (Table 1) indicative of significant OM content. Ro is pivotal in assessing the maturity of source rocks, offering essential clues about their development phase, notably whether they're immature or experiencing early maturity. For

TABLE 1 | X-ray diffraction, total organic carbon (TOC) content and the vitrinite reflectance (Ro) values of the tested shale samples.

Samples	Depth (m)	Minerals composition (wt%)									Geochemistry characteristics	
		Quartz	K-feldspar	Plagioclase	Dolomite	Calcite	Siderite	Pyrite	Clay	Other minerals	TOC (wt%)	Ro (%)
S-1	3530.75	7.1	2.5	6.4	32.5	11.4	3.5	2.2	34.4	—	3.2	0.73
S-2	3551.56	18.1	1.8	4.2	15.9	9.1	5.7	3.0	42.2	—	2.6	0.81
S-3	3558.15	20.0	—	3.5	33.0	4.2	—	3.4	35.0	0.9	2.3	0.73
S-4	3565.50	20.5	—	4.2	6.9	24.6	5.9	4.2	31.0	2.7	2.2	0.70
S-5	3567.50	19.6	—	4.8	—	9.9	11.9	4.7	47.2	1.9	2.0	0.74
S-6	3615.30	9.4	—	5.1	20.0	29.0	—	4.4	32.1	0.0	3.0	0.72
S-7	3636.62	11.5	—	5.5	26.4	6.5	3.0	—	39.5	7.6	2.7	0.83
S-8	3644.10	15.3	—	6.4	12.0	22.0	4.2	4.9	35.2	—	2.2	0.84
S-9	3652.03	12.8	—	4.5	17.4	9.2	3.4	5.3	45.8	1.6	1.9	0.76
S-10	3654.33	8.7	—	4.4	41.3	13.0	1.2	—	26.0	5.4	2.7	0.78
S-11	3660.53	17.9	—	8.4	11.0	6.5	4.1	3.4	48.7	—	2.3	0.83
S-12	3666.83	4.1	2.8	18.5	46.6	4.8	1.4	1.8	18.4	1.6	5.8	0.68
S-13	3670.20	10.3	—	22.9	34.6	1.8	1.2	2.0	19.8	7.4	3.0	0.70
S-14	3677.64	7.3	—	7.4	34.0	22.0	2.7	—	26.6	—	2.3	0.75
S-15	3680.11	10.2	—	16.1	27.3	0.1	6.4	—	30.4	9.5	3.2	0.73
S-16	3686.31	13.1	—	8.6	18.1	5.2	5.1	—	44.3	5.6	1.9	0.69
S-17	3698.76	27.4	—	6.1	6.3	3.2	1.8	4.4	48.8	2.0	2.2	0.76
S-18	3703.61	11.8	2.5	5.8	18.8	—	1.8	8.3	49.3	1.7	2.1	0.80
S-19	3704.60	29.5	—	9.7	—	5.5	0.1	1.7	53.2	0.3	1.0	1.04
S-20	3708.42	23.7	—	3.9	21.5	2.3	1.7	—	44.9	2.0	1.5	0.81

this study, the lacustrine shale samples exhibited Ro values from 0.69% to 1.04% (Table 1), suggesting these samples are mature. The findings from this analysis affirm that the organic matter in the Es_4 lacustrine shale samples has progressed to a low-mature or mature stage.

4.2 | Pore Morphology Characteristics

The shape of the shale pores may be easily seen with FE-SEM. Pyrite pores make up the majority of intercrystalline pores in the research region. Pyrite aggregates have two typical forms, spherical and lens-shaped, with a pore size range of 20–300 nm (Figure 4A). Brittle particles like quartz, feldspar, or calcite, or brittle particles and clay minerals and organic materials, are the primary sites for the development of intergranular pores. The intergranular pores formed between particles such as dolomite and calcite are usually triangular or strip-shaped, with a pore size range of 10–650 nm (Figure 4B). Dissolution pores are mainly in dolomite particles, triangular or circular, often filled with clay minerals or organic matter, with a pore size range of 5–200 nm (Figure 4C). Shale samples with a moderate carbonate concentration and a high abundance of organic materials are more likely to have produced dissolving pores. Within the shale, the organic matter has matured, and many isolated organic pores have formed. Some of the organic pores are filled with solid asphalt. The organic PD is between 200 nm and 12 μm (Figure 4D), which is one of the main types of reservoir space. The lamination plane formed in the sedimentation process of shale naturally has mechanically weak characteristics. Shale forms interlayer fractures under pressure. Shrinkage cracks often appear in groups and spread horizontally in a wavy manner. The cracks are usually half-filled to fully filled with calcite (Figure 4E). Lamination fractures are one of the most typical and common types of microfractures in shale. Structural fractures are relatively rare in clay minerals and often run through the entire field of view in a network (Figure 4F).

An excellent perspective of the morphology of shale pores is offered by FE-SEM. The intercrystalline pores are predominantly pyrite-related. Pyrite aggregates exhibit two distinct forms: spherical and lens-shaped, having pores that range in size from 20 to 300 nm (Figure 4A). The intergranular pores are primarily found between brittle minerals like quartz, feldspar, or calcite, as well as between these minerals and clay or organic matter. Pores formed between particles such as dolomite and calcite often display triangular or strip-like shapes, with sizes varying from 10 to 650 nm (Figure 4B). Dissolution pores, mainly located within dolomite particles, are triangular or circular and frequently filled with clay minerals or organic material, ranging from 5 to 200 nm

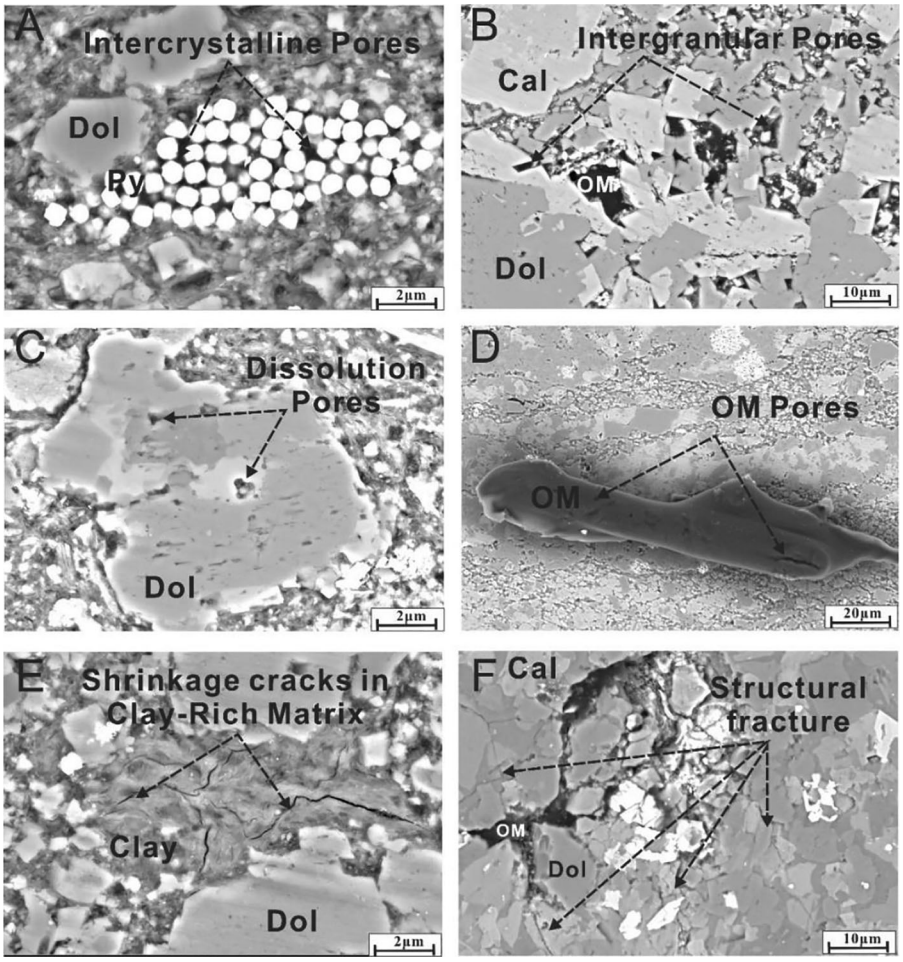

FIGURE 4 | Pore morphology characteristics of the laminated shale in the fourth member Shahejie Formation from the Well S in the study area: (A) SEM showing the intercrystalline pores between pyrite grains, Well S, 3565.5 m; (B) SEM showing the intergranular pores between calcite, dolomite, and organic matter, Well S, 3686.31 m; (C) SEM showing the developed dissolution pores in the dolomite grains, Well S, 3704.6 m; (D) SEM showing the organic matter pores developed, Well S, 3680.11 m; (E) SEM showing the shrinkage cracks in the clay-rich matrix, Well S, 3636.62 m; and (F) SEM showing the structural fracture developed in the dolomite, calcite, and organic matter, Well S, 3698.76 m.

in size (Figure 4C). These dissolution pores are more prevalent in shale samples with high organic matter content and moderate carbonate levels. The organic matter has reached maturity, resulting in the development of numerous isolated organic pores. Some of these pores are partially or fully filled with solid asphalt. Organic pores typically range in diameter from 200 nm to 12 μm (Figure 4D), representing a significant type of reservoir space. The lamination planes formed during shale sedimentation inherently possess mechanically weak characteristics, leading to the formation of interlayer fractures under pressure. Shrinkage cracks often occur in clusters and extend horizontally in a wavy pattern, usually being partially to completely filled with calcite (Figure 4E). Lamination fractures are among the most common and characteristic microfractures in shale. Structural fractures, though less frequent in clay minerals, often form interconnected networks that span the entire field of view (Figure 4F).

4.3 | Quantitative Analyses of Pore Structure

Variations in the nm–μm-scale pore system were revealed by applying CO_2 and N_2 adsorption methods to fully examine the pore structure.

4.3.1 | N_2 Adsorption Isotherms

Figure 5 shows the low-temperature N_2 adsorption/desorption isotherms for the laminated shale samples. The quantities of adsorbed N_2 range widely, from 14.49 to 38.76 g/cm^3 STP. The N_2 adsorption isotherms mostly exhibit a type IV pattern, which is distinguished by a discernible hysteresis loop, in accordance with the IUPAC classification [63, 64].

The observed hysteresis loop is likely caused by capillary condensation occurring within the mesopores, suggesting a significant presence of mesopores in the shale samples. The curve gradually increases, whereas the relative pressure stays below 0.8 during the adsorption process, indicating that adsorption is mostly taking place in the micro- and mesopores. The curve steepens as the relative pressure approaches 1, indicating the presence of macropores in the shale samples. The curve is above the adsorption branch when P/P_0 is higher than 0.45 during the desorption phase. Additionally, the curve closely matches the adsorption branch following a steep fall around $P/P_0 \approx 0.45$.

The geometry of the hysteresis loop provides important information about the pore structure. The 20 shale samples' hysteresis

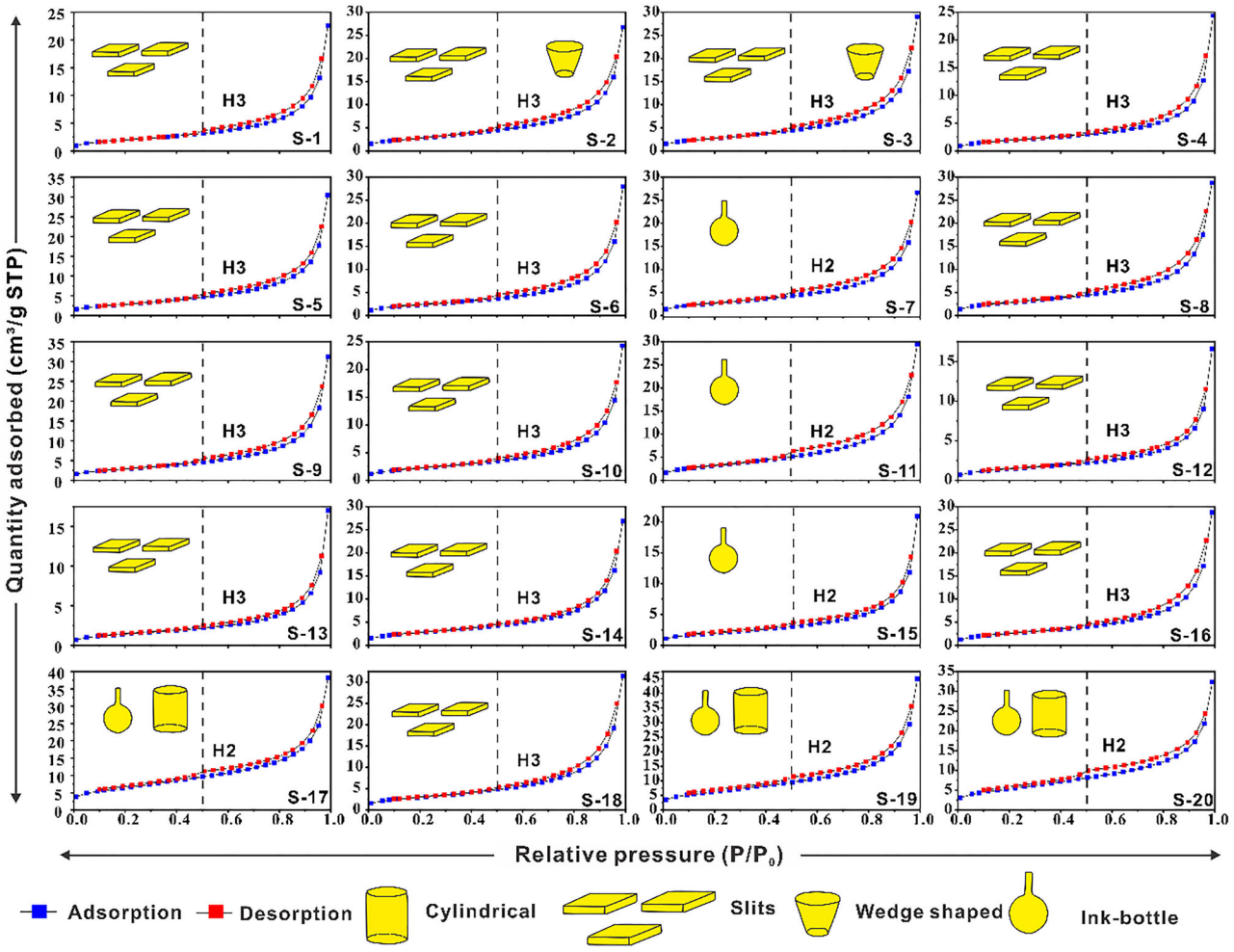

FIGURE 5 | N_2 adsorption–desorption isotherms of the laminated shale in the fourth member Shahejie Formation from the Well S in the study area.

loops may be broadly divided into two groups based on the IUPAC classification: H2 and H3 (Figure 5). H2-type loops usually match mesopores, sometimes referred to as ink-bottle pores, which have larger bodies and thin necks. Conversely, H3-type loops are frequently linked to collections of particles that resemble plates, resulting in the creation of narrow slit-shaped pores. Some shale samples exhibit hysteresis loops that do not precisely fit either H2 or H3 classifications, suggesting a mixture of both pore types in their structures. Laminated shale samples (S-1, S-4, S-5, S-6, S-8, S-9, S-10, S-12, S-13, S-14, S-16, and S-18) predominantly demonstrate H3-type loops, indicating that slit-shaped pores are the dominant type. Conversely, samples S-2 and S-3 exhibit characteristics of H2-type loops, indicating a combination of slit-shaped and ink-bottle pores. Samples S-7, S-11, and S-15 mainly display H2-type loops, suggesting ink-bottle pores as the primary type. Additionally, samples S-17, S-19, and S-20 predominantly exhibit H2-type characteristics, with larger loop sizes indicating the existence of several cylindrical pores, suggesting a significant amount of these samples' open pores. Characterization of slit-shaped and ink-bottle-shaped pore morphologies through N_2 adsorption/desorption isotherms aligns with observations from FE-SEM images in Figure 4. For example, Figure 4B,D depict slit-shaped pores (intergranular and organic matter pores, respectively), whereas Figure 4A,C illustrate ink-bottle-shaped pores (intercrystalline and dissolution pores, respectively). Moreover, the abundance of cylindrical pores is associated with shrinkage cracks (Figure 4E) and structural fractures (Figure 4F) within the laminated shales (Figure 3).

Table 2 presents the BJH-SSA, TPV, and average PD determined from N_2 adsorption. The BJH SSA values range from 5.5278 m^2/g (sample S-13) to 22.4553 m^2/g (sample S-19), with an average of 11.5302 m^2/g across the 20 samples. Regarding BJH TPV, values vary from 0.0258 cm^3/g (sample S-12) to 0.069 cm^3/g (sample S-19), averaging at 0.0432 cm^3/g. The average PD falls within the range of 10.53–20.03 nm, with a mean diameter of 15.87 nm. Analysis of BJH SSA and BJH TPV indicates a prevalence of mesopores over macropores in these samples.

The pore volume distribution curves for each of the 20 laminated shale samples are shown in Figure 6. Using the BJH approach on the N_2 adsorption branch data, the pore size distribution of the shale samples was examined. The PDs, in these samples, range widely, from 1.7 to 300 nm. Furthermore, a majority of the pore size distribution curves exhibit a bimodal pattern with notable peaks at approximately 10–20 and 30–40 nm. Samples S-7, S-11, S-17, S-19, and S-20 demonstrate characteristics of multiple modes, with peaks concentrated around 2–4, 10–20, and 30–40 nm.

TABLE 2 | Analysis results of low-temperature N_2 and CO_2 isothermal adsorption of shale samples.

Samples	Low-temperature N_2 adsorption							Low-temperature CO_2 adsorption		
	BJH SSA (m^2/g)	BJH SSA (m^2/g) >50 nm	BJH SSA (m^2/g) 2–50 nm	BJH TPV (cm^3/g)	BJH TPV (cm^3/g) >50 nm	BJH TPV (cm^3/g) 2–50 nm	BJH average pore width (nm) >2 nm	SSA (m^2/g) <2 nm	TPV (cm^3/g) <2 nm	Average pore width (nm) <2 nm
S-1	8.0059	0.9736	7.0323	0.0351	0.0137	0.0214	17.5387	4.6821	0.0012	0.4221
S-2	11.4540	1.6059	9.8481	0.0417	0.0150	0.0267	14.5542	7.9786	0.0017	0.4125
S-3	11.2834	1.6244	9.6590	0.0452	0.0164	0.0288	16.0077	8.1187	0.0016	0.4262
S-4	7.5455	0.8640	6.6815	0.0378	0.0160	0.0218	20.0344	6.7407	0.0015	0.4251
S-5	11.9209	1.7060	10.2149	0.0472	0.0178	0.0294	15.8388	6.6412	0.0016	0.4103
S-6	9.4883	1.2714	8.2169	0.0433	0.0176	0.0257	18.2625	4.9786	0.0012	0.4142
S-7	10.9925	1.4291	9.5634	0.0414	0.0149	0.0266	15.0825	6.9005	0.0017	0.4141
S-8	11.4036	1.4402	9.9634	0.0447	0.0151	0.0296	15.6852	8.5730	0.0021	0.4085
S-9	11.8091	1.5968	10.2123	0.0484	0.0179	0.0305	16.4042	7.2431	0.0019	0.4098
S-10	8.9620	1.1304	7.8316	0.0378	0.0151	0.0227	16.8629	7.4728	0.0017	0.4164
S-11	13.0958	1.7951	11.3007	0.0458	0.0159	0.0299	13.9997	8.4941	0.0021	0.4201
S-12	5.6713	0.6190	5.0523	0.0258	0.0116	0.0142	18.1946	3.5786	0.0008	0.4153
S-13	5.5278	0.5290	4.9988	0.0265	0.0126	0.0139	19.1397	4.7068	0.0009	0.4308
S-14	10.6119	0.9036	9.7083	0.0419	0.0158	0.0261	15.8045	6.3457	0.0016	0.4021
S-15	7.6405	0.6625	6.9780	0.0326	0.0145	0.0181	17.0689	5.3449	0.0014	0.4121
S-16	10.3044	1.1980	9.1064	0.0447	0.0153	0.0293	17.3363	6.8790	0.0016	0.4286
S-17	21.5850	0.8507	20.7343	0.0578	0.0177	0.0400	10.7054	7.9301	0.0015	0.4252
S-18	12.1632	1.6128	10.5504	0.0489	0.0163	0.0326	16.0831	7.7114	0.0019	0.4128
S-19	22.4553	0.2633	22.1920	0.0690	0.0221	0.0469	12.2975	19.0425	0.0040	0.4140
S-20	18.6838	1.6813	17.0025	0.0492	0.0155	0.0337	10.5275	14.2065	0.0036	0.4080

Abbreviations: BJH, Barrett–Joyner–Halenda; SSA, specific surface area; TPV, total pore volume.

4.3.2 | CO_2 Adsorption Isotherms

Low-temperature CO_2 adsorption is commonly used to examine monolayer adsorption or micropore filling in pores smaller than 2 nm in shale. Figure 7 displays the adsorption isotherms for each of the 20 shale samples. Type I classification for these isotherms means that all the shale samples exhibit microporous characteristics. Sample S-19, with a CO_2 adsorption capacity of 2.19 cm^3/g STP, demonstrates the highest degree of microporosity, whereas sample S-12, with a CO_2 adsorption of 0.45 cm^3/g STP, shows the lowest microporosity.

The micropore volume distribution of each sample was determined using the NLDFT method, and the results are displayed in Figure 8. The shale samples had a wide range of micropore volume distributions, from 0.2 to 0.9 nm. Additionally, the majority of pore size distribution curves show bimodal patterns, with notable peaks found in the 0.45–0.60 and 0.75–0.85 nm ranges. Samples S-1, S-7, S-9, S-11, S-15, and S-20 exhibit multiple modal characteristics, with concentrations observed at 0.3–0.4, 0.45–0.60, and 0.75–0.85 nm.

4.4 | Pore Fractal Characteristics

Figure 9 displays the FHH graphical representations constructed from nitrogen adsorption measurements in shale specimens, plotting $\ln(V/V_0)$ against $\ln(\ln(P_0/P))$. The dimensional parameters (designated as $D1$ and $D2$) were independently derived through linear regression analysis of distinct segments within these plots. Table 3 compiles the calculated gradients from linear approximations, accompanied by determination coefficients ($R^2 > 0.98$ universally) and corresponding scaling parameters. The obtained complexity indices (spanning 2–3) demonstrate that lamellar shale pore networks adhere to fractal scaling principles. Specifically, $D1$ parameters range between 2.3891 and 2.5109, whereas $D2$ measurements occupy the interval 2.5003–2.6681. Significantly, every analyzed specimen exhibited systematically greater $D2$ magnitudes compared to $D1$ values. Statistical analysis reveals no detectable correlation between these dual parameters, implying they quantify independent aspects of rock matrix complexity. This observation diverges from conclusions regarding reservoir shales in lacustrine depositional environments. Such

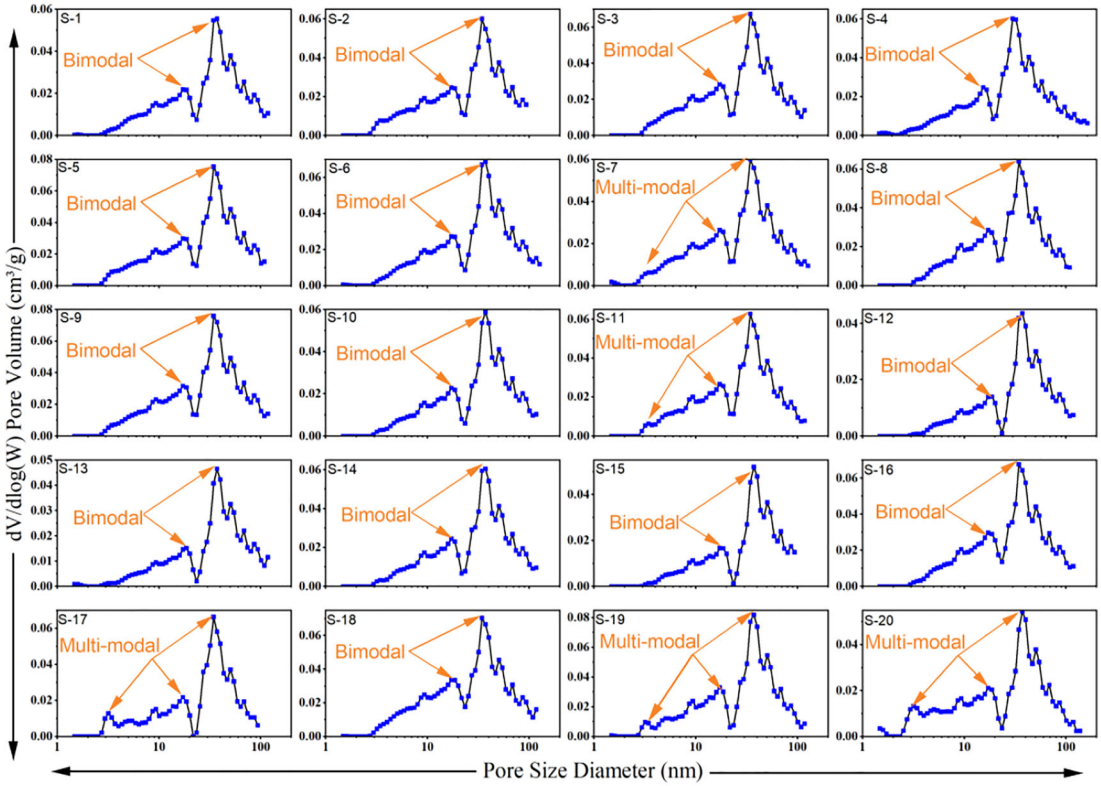

FIGURE 6 | Pore size distributions obtained from low-temperature N_2 adsorption isotherms of the laminated shale in the fourth member Shahejie Formation from the Well S in the study area.

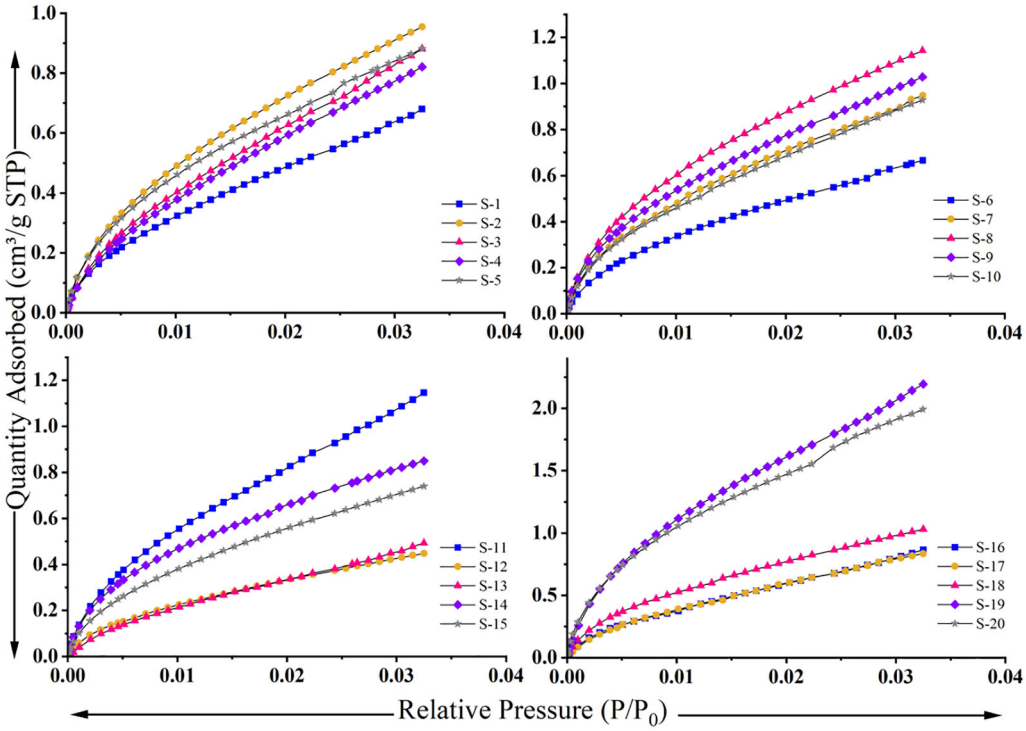

FIGURE 7 | CO_2 adsorption–desorption isotherms of the laminated shale samples in the fourth member Shahejie Formation from the Well S in the study area.

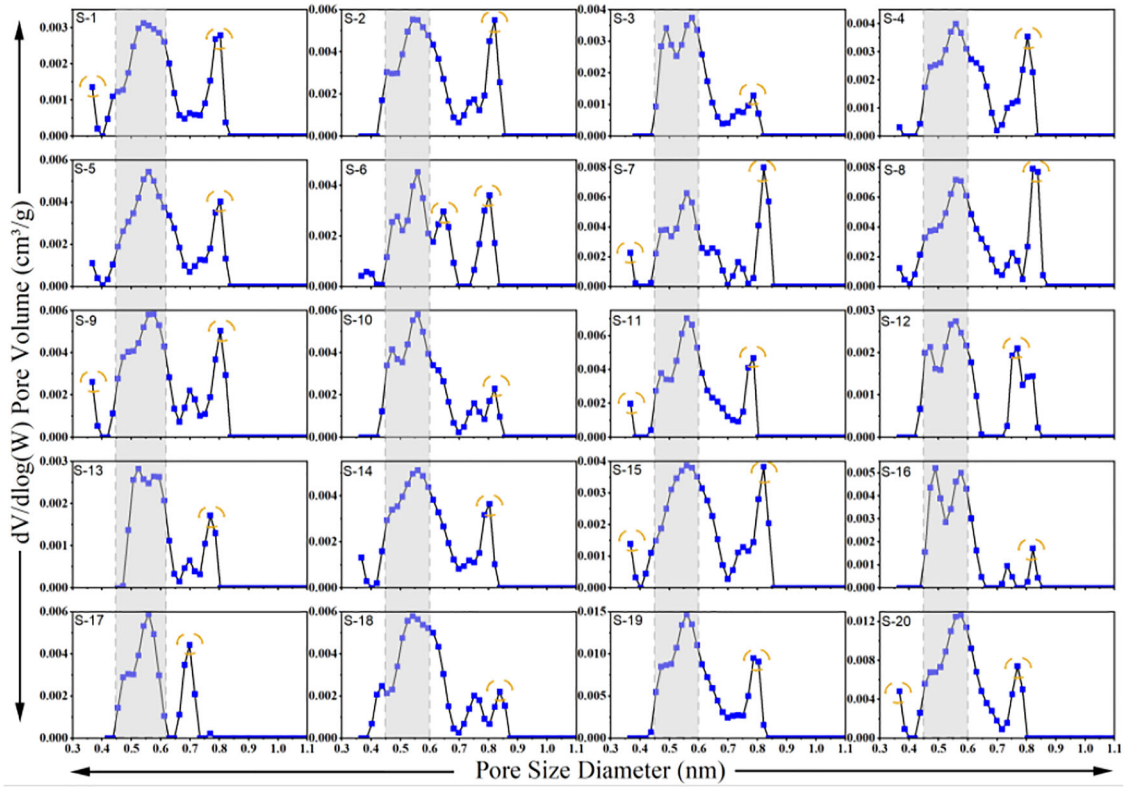

FIGURE 8 | Pore size distributions obtained from lower-temperature CO_2 adsorption isotherms of the laminated shale samples in the fourth member Shahejie Formation from the Well S in the study area.

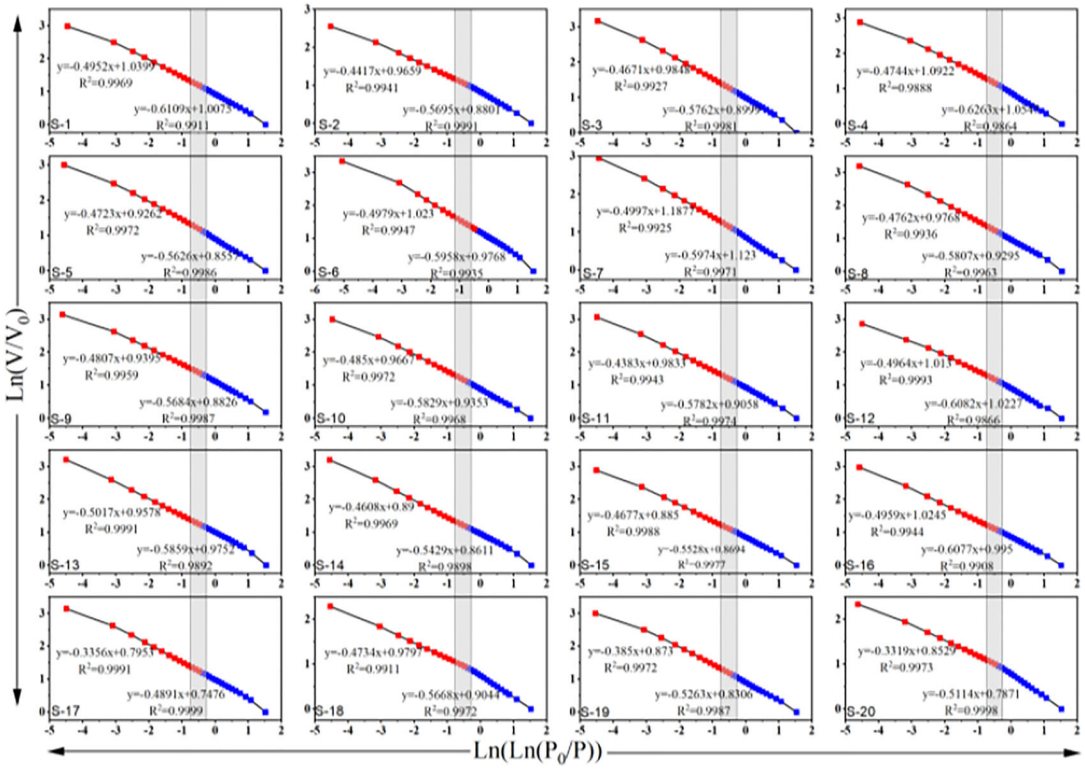

FIGURE 9 | Plots of $\ln(V/V_0)$ versus $\ln(\ln(P_0/P))$ reconstructed from low-temperature N_2 adsorption isotherms of the laminated shale samples in the fourth member Shahejie Formation from the Well S in the study area.

TABLE 3 | Fractal dimensions derived from Frenkel–Halsey–Hill model of the laminated shale samples in the fourth member Shahejie Formation from the Well S.

	P/P_0:0–0.45			P/P_0:0.45–1		
Samples	A_1	R^2	$D_1 = 3 + A_1$	A_2	R^2	$D_2 = 3 + A_2$
S-1	−0.6109	0.9911	2.3891	−0.4952	0.9969	2.5048
S-2	−0.5695	0.9991	2.4305	−0.4417	0.9941	2.5583
S-3	−0.5762	0.9981	2.4238	−0.4671	0.9927	2.5329
S-4	−0.6263	0.9864	2.3737	−0.4744	0.9888	2.5256
S-5	−0.5626	0.9986	2.4374	−0.4723	0.9972	2.5277
S-6	−0.5958	0.9935	2.4042	−0.4979	0.9947	2.5021
S-7	−0.5974	0.9971	2.4026	−0.4997	0.9925	2.5003
S-8	−0.5807	0.9963	2.4193	−0.4762	0.9936	2.5238
S-9	−0.5684	0.9987	2.4316	−0.4807	0.9959	2.5193
S-10	−0.5829	0.9968	2.4171	−0.4850	0.9972	2.5150
S-11	−0.5782	0.9974	2.4218	−0.4383	0.9943	2.5617
S-12	−0.6082	0.9866	2.3918	−0.4964	0.9993	2.5036
S-13	−0.5859	0.9892	2.4141	−0.5017	0.9991	2.4983
S-14	−0.5429	0.9898	2.4571	−0.4608	0.9969	2.5392
S-15	−0.5528	0.9977	2.4472	−0.4677	0.9988	2.5323
S-16	−0.6077	0.9908	2.3923	−0.4959	0.9944	2.5041
S-17	−0.4891	0.9999	2.5109	−0.3356	0.9991	2.6644
S-18	−0.5668	0.9972	2.4332	−0.4734	0.9911	2.5266
S-19	−0.5263	0.9987	2.4737	−0.3850	0.9972	2.6150
S-20	−0.5114	0.9998	2.4886	−0.3319	0.9973	2.6681

dimensional disparity underscores fundamental differences in pore architecture fractalization mechanisms between layered shale systems and conventional reservoir lithologies.

5 | Discussion

5.1 | Pore Structure Distribution Characteristics

The PDs of organic shale vary widely, from nanometers to micrometers. Data on pore structure obtained through N_2 and CO_2 adsorption methods indicate diameters of pores between 0.3 and 300 nm. Figure 10 illustrates the contributions of different pore sizes to TPV and SSA. The primary causes of pore volume are macropores (50–300 nm) and mesopores (2–50 nm), whereas micropores (<2 nm) have a minimal contribution to pore volume (Figure 10A). On the other hand, the biggest contributors to SSA are mesopores and micropores, whereas macropores have the least effect (Figure 10B). The importance of micropores, mesopores, and macropores in shale reservoirs is highlighted by these findings.

The connection between the SSA and TPV of macropores, mesopores, and micropores is shown in Figure 11. A positive correlation is generally observed between the BET SSA and BJH TPV for micropores and mesopores, except for macropores (Figure 11). This pattern aligns with findings from earlier research on marine and lacustrine shales.

5.2 | Pore Structural Parameters and Fractal Dimensions

The correlations between fractal dimensions ($D1$ and $D2$) and pore structure parameters (micropores, mesopores, and macropores) are shown in Figure 12. As the SSA and TPV increase, both fractal dimensions also show an upward trend, indicating that higher SSA and TPV values correspond to larger fractal dimension values (Figure 12). However, PD does not follow the same pattern as the fractal dimensions. The correlation between $D2$ and SSA, TPV, and PD is stronger than that between $D1$, indicating that the irregularity of the pore surface area, total volume, and diameter may be better represented by $D2$. This shows a more significant influence of SSA and TPV on the fractal dimensions.

The negative relationship between $D2$ and PD is more pronounced, whereas $D1$ exhibits a weaker connection with PD (Figure 12), suggesting that $D2$ is a better parameter for describing the irregularity of pore space. Additionally, the relationship between $D1$ and $D2$ is stronger for mesopores than for micropores or macropores, indicating that fractal dimensions are more significantly impacted by mesopore structure. These findings align with the results shown in Figure 10. Laminated shale has the

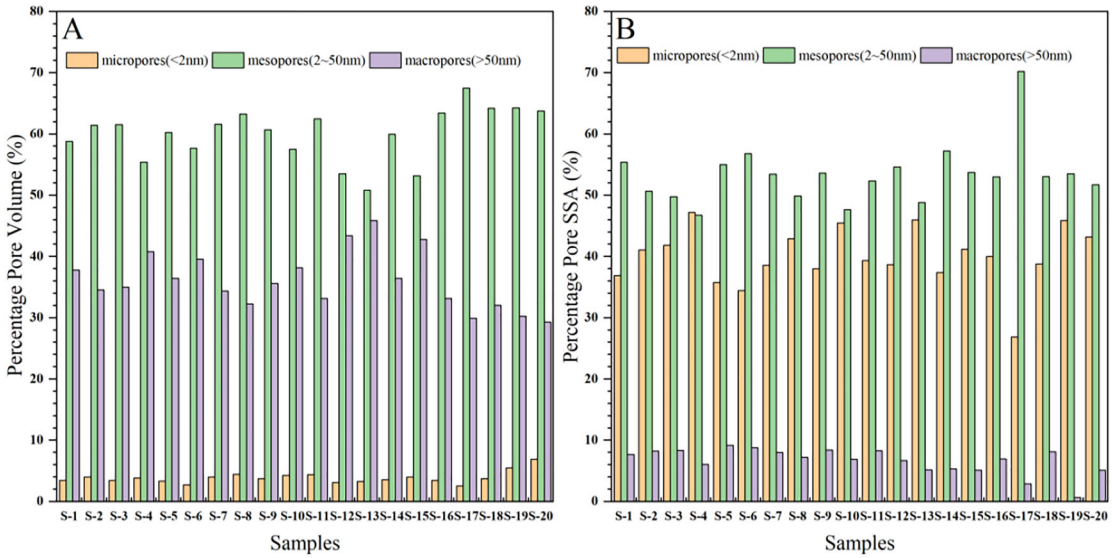

FIGURE 10 | Distributions of different scales of pores acquired from N_2 adsorption and CO_2 adsorption of the laminated shale samples in the fourth member Shahejie Formation from the Well S in the study area: (A) percentage of pore volume and (B) percentage of pore specific surface area. SSA, specific surface area.

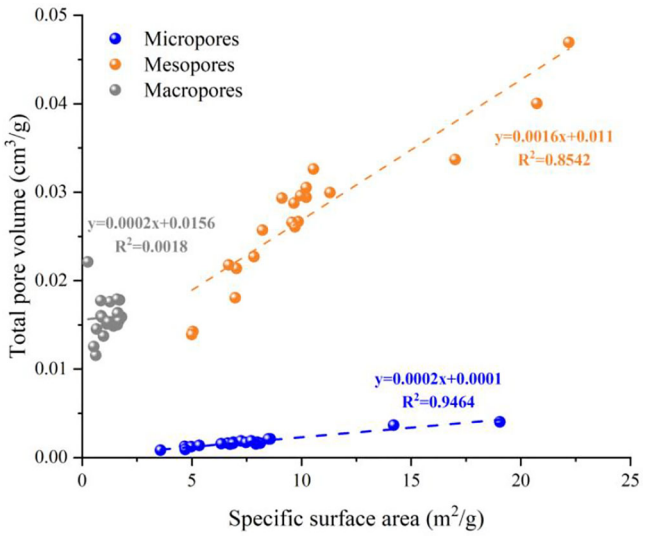

FIGURE 11 | Relationship between the specific surface area (SSA) and total pore volume (TPV) acquired from N_2 adsorption and CO_2 adsorption of the laminated shale samples in the fourth member Shahejie Formation from the Well S in the study area.

same relationships between fractal dimensions and pore structure characteristics as coal, marine shale, and lacustrine shale.

Fractal dimensions of porous materials are typically categorized into pore surface fractal dimension and pore structure fractal dimension, a classification widely adopted in both lacustrine and marine shale studies across different regions. The *D*1 value, calculated from N_2 adsorption data at relative pressures from 0 to 0.45 (correcting the original omission of the lower limit), corresponds to the monolayer adsorption region dominated by Van der Waals forces. Conversely, the *D*2 value, derived from N_2 adsorption data at relative pressures ranging from 0.45 to 1.0, represents the multilayer adsorption region influenced by capillary condensation—this division logic of *D*1/*D*2 based on adsorption mechanisms is consistent with fractal analysis frameworks for shales in the Ordos Basin, Sichuan Basin, and even North America's Marcellus Shale.

*D*1 is defined as the pore surface fractal dimension, where a higher *D*1 value indicates increased irregularity in the pore surface, leading to higher SSA and TPV. This positive correlation is universally validated in studies on lacustrine shales and marine shales [65], reflecting a common feature of shale pore systems. In contrast, *D*2 is considered the pore structure fractal dimension, where a higher *D*2 value signifies greater irregularity in the pore structure and a smaller PD. Our finding differs slightly from research on the lacustrine shales [56], which may be attributed to the higher clay mineral content in the Bohai Bay Basin samples enhancing pore structure irregularity; compared to marine shales with lower *D*2 values, our lacustrine shale samples exhibit higher *D*2 values due to laminated mineralogical heterogeneity.

5.3 | Correlation Between Pore Structure and the Shale Composition

Figure 12 illustrates the impact of various factors such as TOC content, Ro, clay content, quartz content, plagioclase content, dolomite content, and calcite content on parameters like SSA, TPV, PD values, and fractal dimensions.

A notable negative relationship was observed between TOC and the TPV and SSA in micropores, mesopores, and macropores. Specifically, TOC was shown to have a larger negative connection with surface areas ($R^2 = 0.62$) and mesopore volumes ($R^2 = 0.75$). Nevertheless, the surface areas of macropores remained stable despite changes in TOC content. These findings suggest that organic matter negatively impacts micro- and mesopores, likely due to its filling of pores and fractures during early deposition

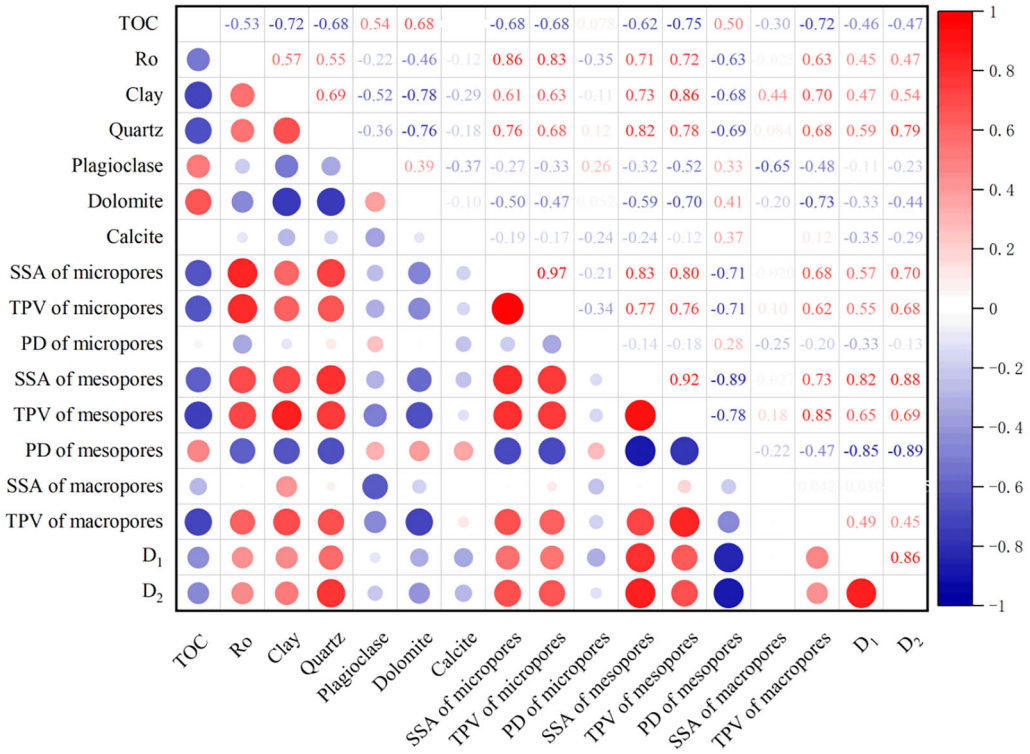

FIGURE 12 | Correlation heatmap in geochemical, mineral parameters with pore structural parameters and fractal dimensions in micropores, mesopores, and macropores of the lacustrine shale samples. PD, pore diameter; Ro, vitrinite reflectance; SSA, specific surface area; TPV, total pore volume.

and diagenesis (Figure 4F). On the other hand, Ro exhibited a strong positive relationship with TPV and SSA in micropores, mesopores, and macropores, with a noteworthy positive association between Ro and both micropore volumes ($R^2 = 0.83$) and surface areas ($R^2 = 0.86$). This correlation is essentially driven by the thermal evolution of organic matter: during the low-maturity to mature stage (Ro 0.6%–1.3%), intensive thermal degradation of kerogen and hydrocarbon expulsion create abundant OM pores; as Ro exceeds 1.3% (high-maturity stage), further cracking of residual OM and bitumen leads to the expansion and connectivity of existing OM pores. Thus, organic matter acts as a significant source of micro–mesopores, with shale having well-developed OM pores (Figure 4D) [66, 67].

The increase in TPV and SSA with higher clay mineral content suggests that clays positively influence the pore system in laminated shale, particularly enhancing pore development. Clay minerals are more critical in mesopore formation compared to micropores and macropores, reflecting their substantial contribution to pore structure. Moreover, clay pores tend to be well-developed around calcite and dolomite grains (Figure 4F) because the stiff carbonate grains form pressure shadows that prevent clay pores from collapsing during mechanical compaction in the early diagenetic stage. Additionally, both TPV and SSA in pores of varying diameter scales show a positive correlation with quartz content. This is attributed to the intergranular pores between detrital quartz grains and the resistance of rigid quartz to compaction—quartz reduces the degree of pore compression during diagenesis, thereby preserving more pore space, which is consistent with previous studies. Quartz minerals particularly contribute more to mesopore development than to micropores or macropores, emphasizing their significant influence on mesopore structure.

Furthermore, TPV and SSA of pores with different diameters show a negative correlation with carbonate content. Although it may seem counterintuitive for a mineral composition to negatively affect TPV and SSA, this is primarily due to chemical cementation during the middle diagenetic stage: Carbonate cements fill primary intergranular pores and secondary OM pores, leading to pore destruction. The negative correlation also stems from the inverse relationship between carbonates and clays, aligning with findings from previous research [68, 69]. No clear correlation was found between TPV and SSA in pores of various diameters and the content of plagioclase or calcite. This suggests that intragranular pores in these minerals are minimal, and most are destroyed by compaction or blocked by clay flocculants and secondary organic matter during diagenesis. Consequently, plagioclase and calcite contribute minimally to pore development in shale reservoirs.

5.4 | Correlation Between Fractal Dimensions and the Shale Composition

To examine how the primary minerals, TOC, and Ro content affect the pore fractal dimensions in laminated shale, the corresponding plots are shown in Figure 12.

There is a negative association found between the values of *D*1 and *D*2 and increasing TOC content, indicating that TOC negatively impacts the pore surface and structure. This indicates that organic

matter fills the pores, reducing their complexity. Conversely, greater Ro content clearly results in greater *D*1 and *D*2 readings, implying that Ro positively influences the fractal dimensions. Elevated Ro typically leads to the formation of numerous organic matter nanopores on the micro- and mesoscale, enhancing the pore system's complexity.

As the amount of quartz increases, so do the fractal dimensions of *D*1 and *D*2, demonstrating that larger quartz concentrations correspond to larger fractal dimension values. Quartz crystals are prone to diagenesis and secondary expansion, and they often contribute to a complex pore structure, resulting in irregularities that elevate the fractal dimension. Fractal dimensions are positively impacted by clays, as evidenced by the fact that both *D*1 and *D*2 values increase with clay mineral concentration. Different pore types are contributed by shale varieties that include different kinds of clay minerals. This results in a more irregular pore structure and, ultimately, larger fractal dimensions. However, no significant trend is observed in the *D*1 and *D*2 values with increasing plagioclase, dolomite, or calcite content, suggesting that these minerals have minimal effect on the pore surface and structure.

6 | Conclusion

An inaccurate assessment of the pore system in laminated shale formations could significantly limit the resource potential in oil reservoirs. This study thoroughly evaluated the pore structure at the nm–μm scale, along with its fractal dimensions and development-influencing factors, focusing on the Paleogene Shahejie Formation lacustrine shale oil in the Bohai Bay Basin to illustrate pore characteristics across different laminae. The findings enhance the understanding of shale resource potential and provide critical guidance for identifying optimal shale oil zones, challenging the conventional view that laminated shale reservoirs inherently have low anticipated final recovery. Key findings reveal that the primary pores in laminated shales are matrix-related inorganic pores (intercrystalline, intergranular, dissolution pores, and microfractures) rather than organic-matter-dominated pores, highlighting the key role of inorganic pores in forming production sweet spots. The PD of these shales is primarily concentrated in the 2–40 nm range, contradicting earlier research that emphasized smaller (0.4–20 nm) pores as more influential for shale oil production. Additionally, high clay and quartz mineral contents (sum > 70%) in laminated shales significantly enhance micro–mesopore structure and complexity, which is a critical indicator for sweet spot identification. To strengthen the guiding significance for exploration and development, we propose specific sweet spot prediction criteria: high clay–quartz content, PD concentrated in 2–40 nm, and moderate thermal maturity (Ro = 0.6%–1.3%, balancing pore development and hydrocarbon retention). For engineering practices, targeted fracturing strategies focusing on laminated interfaces are recommended to maximize the connectivity of matrix-dominated inorganic pores, given the minimal contribution of organic-matter pores. A verifiable scientific hypothesis is put forward: The fractal dimension *D*2 (characterizing pore structure complexity) positively correlates with fracturing stimulation efficiency. Although this study provides geological examples, molecular dynamics simulations were unsuccessful in uncovering micro–nanoscale pore generation mechanisms. Future research should focus on three directions: Coupling nanoscale diagenetic processes with pore evolution, developing effective molecular dynamics simulation methods for inorganic pore formation, and conducting dynamic oil migration experiments in matrix-dominated pore systems. These efforts will refine recovery prediction models and further improve the exploration and development efficiency of lacustrine shale oil.

Acknowledgments

This work was financially supported by the National Natural Science Foundation of China (Grant Number 42072150) and China Scholarship Council (Grant Number CSC202306440132) for the financial support provided to Biao Sun. We thank the sponsors of this project.

Conflicts of Interest

The authors declare no conflicts of interest.

Data Availability Statement

Data will be made available on request.

References

1. Y. Li, D. Chen, F. Jiang, et al., "Differential Enrichment of Middle-Low Maturity Lacustrine Shale Oil in the Late Eocene Shahejie Formation, Bohai Bay Basin," *Marine and Petroleum Geology* 172 (2025): 107217, https://doi.org/10.1016/j.marpetgeo.2024.107217.

2. J. Xu, Q. Wu, X. Cheng, et al., "Micro-Charging and Accumulation of Shale Oil in Lamellar Shale Interbedded With Siltstones, Dongying Depression, Bohai Bay Basin," *Marine and Petroleum Geology* 174 (2025): 107298, https://doi.org/10.1016/j.marpetgeo.2025.107298.

3. Y. Song, Z. Song, Y. Mo, et al., "Maturity-Dependent Thermodynamic and Flow Characteristics in Continental Shale Oils," *Energy* 318 (2025): 134867, https://doi.org/10.1016/j.energy.2025.134867.

4. W. Zhao, W. Liu, C. Bian, et al., "Role of Preservation Conditions on Enrichment and Fluidity Maintenance of Medium to High Maturity Lacustrine Shale Oil," *Petroleum Exploration and Development* 52 (2025): 1–16, https://doi.org/10.1016/S1876-3804(25)60001-2.

5. J.-H. Lv, T. Hu, W. Zhang, et al., "Microscopic Oil Occurrence in the Permian Alkaline Lacustrine Shales: Fengcheng Formation, Mahu Sag, Junggar Basin," *Petroleum Science* 22 (2025): 1407–1427, https://doi.org/10.1016/j.petsci.2025.01.005.

6. B. Sun, X. Liu, J. Liu, et al., "The Heterogeneity of Lithofacies Types, Combination Modes, and Sedimentary Model of Lacustrine Shale Restricted by High-Frequency Sequence," *Geological Journal* 57 (2022): 4035–4051, https://doi.org/10.1002/gj.4526.

7. S. Wang, M. Zhang, Y. Zhang, et al., "Mechanisms of CO_2 Huff and Puff Enhanced Oil Recovery and Storage Within Shale Nanopores," *Chemical Engineering Journal* 506 (2025): 160098, https://doi.org/10.1016/j.cej.2025.160098.

8. Y. Huang, F. Liu, Y. Kang, Y. Hu, L. Li, and Y. Liu, "Experimental Study on CO_2 Huff-n-Puff for Enhanced Shale Oil Recovery and Microscopic Mobilization Characteristics Using Online NMR," *Fuel* 387 (2025): 134428, https://doi.org/10.1016/j.fuel.2025.134428.

9. Y. Chi, B. Liu, L. Bai, Y. Su, Y. Huo, and E. Mohammadian, "Determination of Oil Contents in Ultralow Temperature Samples in High Maturity Shales Using 2D NMR Fluid Evaluation Technology," *Marine and Petroleum Geology* 174 (2025): 107304, https://doi.org/10.1016/j.marpetgeo.2025.107304.

10. B. Sun, X.-P. Liu, J. Liu, T. Liu, Z.-X. Hua, and W.-D. Peng, "Evolution and Generation Mechanism of Retained Oil in Lacustrine Shales: A Combined ReaxFF-MD and Pyrolysis Simulation Perspective," *Petroleum Science* 22 (2025): 29–41, https://doi.org/10.1016/j.petsci.2024.07.020.

11. S. Wang, G. Wang, L. Huang, et al., "Logging Evaluation of Lamina Structure and Reservoir Quality in Shale Oil Reservoir of Fengcheng Formation in Mahu Sag, China," *Marine and Petroleum Geology* 133 (2021): 105299, https://doi.org/10.1016/j.marpetgeo.2021.105299.

12. K. Xi, K. Li, Y. Cao, et al., "Laminae Combination and Shale Oil Enrichment Patterns of Chang 73 Sub-Member Organic-Rich Shales in the Triassic Yanchang Formation, Ordos Basin, NW China," *Petroleum Exploration and Development* 47 (2020): 1342–1353, https://doi.org/10.1016/S1876-3804(20)60142-8.

13. K. Li, K. Xi, Y. Cao, X. Shan, and M. Lin, "Diagenetic Alterations Induced by Lamina-Scale Mass Transfer and the Impacts on Shale Oil Reservoir Formation in Carbonate-Rich Shale of the Permian Lucaogou Formation, Jimusar Sag," *Marine and Petroleum Geology* 162 (2024): 106709, https://doi.org/10.1016/j.marpetgeo.2024.106709.

14. B. Sun, X. Liu, and X. Zhao, "Laminated Shale Oil System Mobility and Controlling Factors of the Paleogene Shahejie Formation: Evidences From T1-T2 NMR Experiments, Multi-Temperature Pyrolysis and Confocal Laser Scanning Microscopy," *Fuel* 379 (2025): 133015, https://doi.org/10.1016/j.fuel.2024.133015.

15. X. Wang, E. L. Grossman, and M. R. Becker, "High-Resolution Chemofacies and Pore System Characterization of the Pennsylvanian Cline Shale, Midland Basin, Texas," *Marine and Petroleum Geology* 170 (2024): 107120, https://doi.org/10.1016/j.marpetgeo.2024.107120.

16. Y.-J. Ren, B. Wei, B.-X. Ji, et al., "Pore-scale Probing CO_2 Huff-n-Puff in Extracting Shale Oil From Different Types of Pores Using Online T1–T2 Nuclear Magnetic Resonance Spectroscopy," *Petroleum Science* 21 (2024): 4119–4129, https://doi.org/10.1016/j.petsci.2024.07.001.

17. H. Zheng, F. Yang, Q. Guo, and K. Liu, "Upscaling Characterizing Pore Connectivity, Morphology and Orientation of Shale From Nano-Scale to Micro-Scale," *Marine and Petroleum Geology* 172 (2025): 107213, https://doi.org/10.1016/j.marpetgeo.2024.107213.

18. G. Wang, Z. Jin, and Q. Zhang, "Characterization of Pore Structure Before and After Solvent Extraction: A Case Study of Lacustrine Shales in the Triassic Chang 7 Formation, Ordos Basin, Northern China," *Journal of Asian Earth Sciences* 282 (2025): 106526, https://doi.org/10.1016/j.jseaes.2025.106526.

19. X. Chen, X. Qu, and S. Xu, "Dissolution Pores in Shale and Their Influence on Reservoir Quality in Damintun Depression, Bohai Bay Basin, East China: Insights From SEM Images, N_2 Adsorption and Fluid-Rock Interaction Experiments," *Marine and Petroleum Geology* 117 (2020): 104394, https://doi.org/10.1016/j.marpetgeo.2020.104394.

20. T. Guo, H. Deng, S. Zhao, L. Wei, and J. He, "Formation Mechanisms and Exploration Breakthroughs of New Type of Shale Gas in Cambrian Qiongzhusi Formation, Sichuan Basin, SW China," *Petroleum Exploration and Development* 52 (2025): 64–78, https://doi.org/10.1016/S1876-3804(25)60005-X.

21. L.-H. Bai, B. Liu, Y.-J. Du, et al., "Distribution Characteristics and Oil Mobility Thresholds in Lacustrine Shale Reservoir: Insights From N_2 Adsorption Experiments on Samples Prior to and Following Hydrocarbon Extraction," *Petroleum Science* 19 (2022): 486–497, https://doi.org/10.1016/j.petsci.2021.10.018.

22. B. Sun, X.-P. Liu, J. Liu, et al., "Lacustrine Shale Oiliness Influenced by Diabase Intrusions in the Paleogene Funing Formation, Subei Basin, China," *Petroleum Science* 20 (2023): 2683–2694, https://doi.org/10.1016/j.petsci.2023.05.013.

23. K. Liu, N. Zakharova, A. Adeyilola, T. Gentzis, H. Carvajal-Ortiz, and H. Fowler, "Understanding the CO_2 Adsorption Hysteresis Under Low Pressure: An Example From the Antrim Shale in the Michigan Basin: Preliminary Observations," *Journal of Petroleum Science & Engineering* 203 (2021): 108693, https://doi.org/10.1016/j.petrol.2021.108693.

24. D. Wang, H. Hu, T. Wang, et al., "Difference Between of Coal and Shale Pore Structural Characters Based on Gas Adsorption Experiment and Multifractal Analysis," *Fuel* 371 (2024): 132044, https://doi.org/10.1016/j.fuel.2024.132044.

25. C. R. Clarkson, N. Solano, R. M. Bustin, et al., "Pore Structure Characterization of North American Shale Gas Reservoirs Using USANS/SANS, Gas Adsorption, and Mercury Intrusion," *Fuel* 103 (2013): 606–616, https://doi.org/10.1016/j.fuel.2012.06.119.

26. J. Li, M. Wang, and W. Jia, "A Modified Surface to Volume (SVR) Method to Calculate Nuclear Magnetic Resonance (NMR) Surface Relaxivity: Theory and a Case Study in Shale Reservoirs," *Marine and Petroleum Geology* 170 (2024): 107159, https://doi.org/10.1016/j.marpetgeo.2024.107159.

27. C. Li, M. Tan, Z. Wang, Y. Li, and L. Xiao, "Nuclear Magnetic Resonance Pore Radius Transformation Method and Fluid Mobility Characterization of Shale Oil Reservoirs," *Geoenergy Science and Engineering* 221 (2023): 211403, https://doi.org/10.1016/j.geoen.2022.211403.

28. P. Zhang, H. Wu, S. Lu, et al., "The Occurrence of Pore Fluid in Shale-Oil Reservoirs Using Nuclear Magnetic Resonance: The Paleogene Funing Formation, Subei Basin, Eastern China," *Marine and Petroleum Geology* 167 (2024): 106986, https://doi.org/10.1016/j.marpetgeo.2024.106986.

29. W. Yang, R. Yang, M. Wang, et al., "Impact of Lithofacies Categories on Inflection-Point Behaviors in Micro-Nano Pore-Structure Evolution: Implications for Differential Reservoir-Forming Mechanisms and "Sweet-Spot Intervals" Identification for Marine Gas Shales," *Marine and Petroleum Geology* 176 (2025): 107336, https://doi.org/10.1016/j.marpetgeo.2025.107336.

30. J. Wan, Z. Yu, Y. Yuan, M. Sun, W. Huang, and R. Rezaee, "Laminae in Multiple Lithofacies and Impact on Pore Structures in Lacustrine Shale: The Cretaceous Qingshankou Formation, Songliao Basin," *Marine and Petroleum Geology* 174 (2025): 107321, https://doi.org/10.1016/j.marpetgeo.2025.107321.

31. N. Zhang, X. Wang, S. Wang, et al., "Multifractal Characteristics on Pore Structure of Longmaxi Shale Using Nuclear Magnetic Resonance (NMR)," *Geoenergy Science and Engineering* 241 (2024): 213176, https://doi.org/10.1016/j.geoen.2024.213176.

32. H. Wang, W. Wu, T. Chen, J. Yu, and J. Pan, "Pore Structure and Fractal Analysis of Shale Oil Reservoirs: A Case Study of the Paleogene Shahejie Formation in the Dongying Depression, Bohai Bay," *Journal of Petroleum Science and Engineering* 177 (2019): 711–723, https://doi.org/10.1016/j.petrol.2019.02.081.

33. X. Liu, J. Liu, X. Wang, et al., "Mechanisms of Fine-Grained Sedimentation and Reservoir Characteristics of Shale Oil in Continental Freshwater Lacustrine Basin: A Case Study From Chang 73 Sub-Member of Triassic Yanchang Formation in Southwestern Ordos Basin, NW China," *Petroleum Exploration and Development* 52 (2025): 95–111, https://doi.org/10.1016/S1876-3804(25)60007-3.

34. X. Pang, G. Wang, L. Kuang, et al., "Lamellation Fractures in Shale Oil Reservoirs: Recognition, Prediction and Their Influence on Oil Enrichment," *Marine and Petroleum Geology* 148 (2023): 106032, https://doi.org/10.1016/j.marpetgeo.2022.106032.

35. S. Hui, X. Pang, Z. Chen, et al., "Quantifying the Relative Contribution and Evolution of Pore Types to Shale Reservoir Space: Constraints From Over-Mature Marine Shale in the Sichuan Basin, SW China," *Journal of Asian Earth Sciences* 249 (2023): 105625, https://doi.org/10.1016/j.jseaes.2023.105625.

36. Y. Huang, G. Wang, Y. Zhang, et al., "Logging Evaluation of Pore Structure and Reservoir Quality in Shale Oil Reservoir: The Fengcheng Formation in Mahu Sag, Junggar Basin, China," *Marine and Petroleum Geology* 156 (2023): 106454, https://doi.org/10.1016/j.marpetgeo.2023.106454.

37. Q. Mei, R. Guo, X. Zhou, et al., "Pore Structure Characteristics and Impact Factors of Laminated Shale Oil Reservoir in Chang 73 Sub-

Member of Ordos Basin, China," *Journal of Natural Gas Geoscience* 8 (2023): 227–243, https://doi.org/10.1016/j.jnggs.2023.07.003.

38. Z. Ma, L. Zheng, X. Xu, F. Bao, and X. Yu, "Thermal Simulation Experiment of Organic Matter-Rich Shale and Implication for Organic Pore Formation and Evolution," *Petroleum Research* 2 (2017): 347–354, https://doi.org/10.1016/j.ptlrs.2017.04.005.

39. L. Wang, B. Liu, L.-H. Bai, et al., "Maceral Evolution of Lacustrine Shale and Its Effects on the Development of Organic Pores During Low Mature to High Mature Stage: A Case Study From the Qingshankou Formation in Northern Songliao Basin, Northeast China," *Petroleum Science* 20 (2023): 2709–2725, https://doi.org/10.1016/j.petsci.2023.08.025.

40. C. Hu, J. Tan, Q. Lyu, and Y. Zhang, "Evolution of Organic Pores in Permian Low Maturity Shales From the Dalong Formation in the Sichuan Basin: Insights From a Thermal Simulation Experiment," *Gas Science and Engineering* 121 (2024): 205166, https://doi.org/10.1016/j.jgsce.2023.205166.

41. T. Liu, X. Liu, and B. Sun, "Evolution Characteristics of a Laminated Retained Oil System: Insights From Semi-Closed Hydrous Pyrolysis Experiments," *Fuel* 389 (2025): 134532, https://doi.org/10.1016/j.fuel.2025.134532.

42. A. Ari and S. Akbulut, "Investigation of Sand-Geomaterial Interface Response Using Fractal Theory: Particle Shape, Gradation and Surface Roughness Effects," *Advanced Powder Technology* 36 (2025): 105072, https://doi.org/10.1016/j.apt.2025.105072.

43. V. K. Mishra, V. A. Mendhe, A. D. Kamble, S. Pandey, V. P. Singh, and P. Shukla, "Significance of Organo-Mineralogical Constituents on Pore Distribution, Fractals and Gas Sorption Mechanism of Permian Shale Beds in Korba Sub-Basin of the Son-Mahanadi Valley, India," *Geoenergy Science and Engineering* 231 (2023): 212334, https://doi.org/10.1016/j.geoen.2023.212334.

44. F. Chen, Q. Zheng, X. Ding, S. Lu, and H. Zhao, "Pore Size Distributions Contributed by OM, Clay and Other Minerals in Over-Mature Marine Shale: A Case Study of the Longmaxi Shale From Southeast Chongqing, China," *Marine and Petroleum Geology* 122 (2020): 104679, https://doi.org/10.1016/j.marpetgeo.2020.104679.

45. F. Wang, Z. Feng, X. Wang, and H. Zeng, "Effect of Organic Matter, Thermal Maturity and Clay Minerals on Pore Formation and Evolution in the Gulong Shale, Songliao Basin, China," *Geoenergy Science and Engineering* 223 (2023): 211507, https://doi.org/10.1016/j.geoen.2023.211507.

46. Z. Song, J. Zhang, and S. Jin, "The Occurrences and Mobility of Shale Oil in the Pore Space of Terrestrial Shale," *Fuel* 374 (2024): 132377, https://doi.org/10.1016/j.fuel.2024.132377.

47. W. Zhang, S. Zhou, Z. Yu, et al., "Controls of Clay Mineral Transformation and Organic Matter on Pore Networks of the Paleogene Lacustrine Shale Oil System in the Yitong Basin, NE China," *Journal of Asian Earth Sciences* 280 (2025): 106469, https://doi.org/10.1016/j.jseaes.2024.106469.

48. J. Chang, X. Fan, Z. Jiang, et al., "Differential Impact of Clay Minerals and Organic Matter on Pore Structure and Its Fractal Characteristics of Marine and Continental Shales in China," *Applied Clay Science* 216 (2022): 106334, https://doi.org/10.1016/j.clay.2021.106334.

49. D. Zhang, Y. Chen, S. Ji, et al., "Analyses of the Characteristics and Main Controlling Factors of Shale Pores in the Niutitang Formation in the Guizhou Region," *Natural Gas Industry B* 11 (2024): 394–404, https://doi.org/10.1016/j.ngib.2024.08.006.

50. J. Wan, Z. Yu, Y. Yuan, W. Huang, Z. Dong, and R. Rezaee, "Lithofacies Classification and Reservoir Property of Lacustrine Shale, the Cretaceous Qingshankou Formation, Songliao Basin, Northeast China," *Marine and Petroleum Geology* 173 (2025): 107262, https://doi.org/10.1016/j.marpetgeo.2024.107262.

51. P. Gao, X. Xiao, G. Meng, G. G. Lash, S. Li, and Y. Han, "Quartz Types and Origins of the Upper Permian Dalong Formation Shale of the Sichuan Basin: Implications for Pore Preservation in Deep Shale Reservoirs," *Marine and Petroleum Geology* 156 (2023): 106461, https://doi.org/10.1016/j.marpetgeo.2023.106461.

52. Q. Gou, S. Xu, F. Hao, L. Zhang, Z. Chen, and N. Bai, "Petrography and Mineralogy Control the Nm-μm-Scale Pore Structure of Saline Lacustrine Carbonate-Rich Shales From the Jianghan Basin, China," *Marine and Petroleum Geology* 155 (2023): 106399, https://doi.org/10.1016/j.marpetgeo.2023.106399.

53. X. Song, X. Fu, H. Li, et al., "Improved Method for Quantitative Fault Sealing Evaluation in Sand-Clay Sequences: A Case Study From the West Subsag of Bozhong Sag in the Bohai Bay Basin, China," *Marine and Petroleum Geology* 169 (2024): 107062, https://doi.org/10.1016/j.marpetgeo.2024.107062.

54. L. Pei, X. Wang, G. Gao, and W. Liu, "Geochemical Heterogeneity, Origin and Secondary Alteration of Natural Gas Inside and Outside Buried Hills of Xinglongtai Area, West Sag, Liaohe Depression, Bohai Bay Basin," *Journal of Petroleum Science & Engineering* 208 (2022): 109456, https://doi.org/10.1016/j.petrol.2021.109456.

55. H. Li, B. Liu, X. Liu, L. Meng, L. Cheng, and H. Wang, "Mineralogy and Inorganic Geochemistry of the Es4 Shales of the Damintun Sag, Northeast of the Bohai Bay Basin: Implication for Depositional Environment," *Marine and Petroleum Geology* 110 (2019): 886–900, https://doi.org/10.1016/j.marpetgeo.2019.09.002.

56. H. Li, S. He, A. E. Radwan, J. Xie, and Q. Qin, "Quantitative Analysis of Pore Complexity in Lacustrine Organic-Rich Shale and Comparison to Marine Shale: Insights From Experimental Tests and Fractal Theory," *Energy & Fuels* 38 (2024): 16171–16188, https://doi.org/10.1021/acs.energyfuels.4c03095.

57. M. Du, Y. Zhengming, W. Lv, et al., "Experimental Study on Microscopic Production Characteristics and Influencing Factors During Dynamic Imbibition of Shale Reservoir With Online NMR and Fractal Theory," *Energy* 310 (2024): 133244, https://doi.org/10.1016/j.energy.2024.133244.

58. J. Zhang, X. Xiao, and J. Wang, "Pore Structure and Fractal Characteristics of Coal-Bearing Cretaceous Nenjiang Shales From Songliao Basin, Northeast China," *Journal of Natural Gas Geoscience* 9 (2024): 197–208, https://doi.org/10.1016/j.jnggs.2024.03.005.

59. J. Zhang, Y. Tang, D. He, P. Sun, and X. Zou, "Full-Scale Nanopore System and Fractal Characteristics of Clay-Rich Lacustrine Shale Combining FE-SEM, Nano-CT, Gas Adsorption and Mercury Intrusion Porosimetry," *Applied Clay Science* 196 (2020): 105758, https://doi.org/10.1016/j.clay.2020.105758.

60. Y. Nakajima and H. Takahasi, "Density Combinatorics Theorems in Fractal Dimension Theory of Continued Fractions," *Advances in Mathematics* 482 (2025): 110635, https://doi.org/10.1016/j.aim.2025.110635.

61. A. Khalili Golmankhaneh, C. Cattani, H. Kalita, S. Furuichi, and P. E. T. Jørgensen, "Fractal Green Function Theory," *Communications in Nonlinear Science and Numerical Simulation* 152 (2026): 109402, https://doi.org/10.1016/j.cnsns.2025.109402.

62. K. Luo, "Hierarchical Synchronization and Distortion Scaling in Social Media Networks: A Fractal-Like Topology Theory," *Chaos, Solitons & Fractals* 202 (2026): 117581, https://doi.org/10.1016/j.chaos.2025.117581.

63. Z. Tong, J. Zhang, Z. Li, Y. Wu, D. Wang, and D. Gong, "Investigation of Organic-Shale Nanopores in the Lower Cambrian Niutitang Formation Using Low Temperature N_2 and CO_2 Adsorption: Multifractality and Classification," *Microporous and Mesoporous Materials* 337 (2022): 111935, https://doi.org/10.1016/j.micromeso.2022.111935.

64. X. Song, X. Zhou, and X. Lv, "Quantitative Evaluation of Pore Connectivity of Shales With a Type H3 Sorption Hysteresis Loop," *Journal of Asian Earth Sciences* 247 (2023): 105595, https://doi.org/10.1016/j.jseaes.2023.105595.

65. H. Li, Z. Xu, X. Gao, et al., "Pore Structure Evolution and Geological Controls in Lacustrine Shale Systems With Implications for Marine Shale Reservoir Characterization," *Scientific Reports* 15 (2025): 17702, https://doi.org/10.1038/s41598-025-02415-y.

66. Y. Zhang, S. Hu, C. Shen, Z. Liao, J. Xu, and X. Zhang, "Factors Influencing the Evolution of Shale Pores in Enclosed and Semi-Enclosed

Thermal Simulation Experiments, Permian Lucaogou Formation, Santanghu Basin, China," *Marine and Petroleum Geology* 135 (2022): 105421, https://doi.org/10.1016/j.marpetgeo.2021.105421.

67. M. Shi, B. Yu, J. Zhang, H. Huang, Y. Yuan, and B. Li, "Evolution of Organic Pores in Marine Shales Undergoing Thermocompression: A Simulation Experiment Using Hydrocarbon Generation and Expulsion," *Journal of Natural Gas Science and Engineering* 59 (2018): 406–413, https://doi.org/10.1016/j.jngse.2018.09.008.

68. X. Wang, X. Kong, Q. Liu, et al., "Effect of Clay Minerals on Carbonate Precipitation Induced by *Cyanobacterium synechococcus* sp.," *Microbiology Spectrum* 11 (2023): e0036323, https://doi.org/10.1128/spectrum.00363-23.

69. H. Liu, Y. Bao, S. Zhang, et al., "Structural Characteristics of Continental Carbonate-Rich Shale and Shale Oil Movability: A Case Study of the Paleogene Shahejie Formation Shale in Jiyang Depression, Bohai Bay Basin, China," *Petroleum Exploration and Development* 50 (2023): 1320–1332, https://doi.org/10.1016/S1876-3804(24)60469-6.